

Theoretical model for the extreme positive magnetoresistance

George Kastinakis

Institute of Electronic Structure and Laser (IESL),

*Foundation for Research and Technology - Hellas (FORTH), P.O. Box 1527, Iraklio, Crete 71110, Greece**

(Dated: 9 June 2023)

We present a model for the positive extreme magnetoresistance (XMR), recently observed in a plethora of metallic systems, such as PtSn₄, PtBi₂, PdCoO₂, WTe₂, NbSb₂, NbP, TaSb₂, LaSb, LaBi, ZrSiS and MoTe₂. The model is an extension of our earlier work on positive giant magnetoresistance, and uses an elaborate diagrammatic formulation. XMR is a bulk effect (not a surface effect), due to the dramatic sensitivity of the conductivity to the finite magnetic field H . This is possible at low temperatures, in the presence of finite disorder elastic spin scattering, and for a special value, predicted from the theory, of the material-dependent effective Coulomb repulsion. Good agreement with experiments is obtained. According to our model XMR is higher in cleaner samples, and anisotropic with regards to the direction of H . We discuss in particular compounds containing the elements Pt, Sc, and Rh.

PACS numbers: 72.10.-d, 72.10.Di, 72.15.Rn

1. Introduction

Positive extreme magnetoresistance (XMR) has been observed in several semimetallic systems like PtSn₄ [1], PdCoO₂ [2], WTe₂ [3, 4], NbSb₂ [5], NbP [6], TaSb₂ [7], LaSb [8–11], LaBi [10, 12], MoTe₂ [13], ZrSiS [14–16], and PtBi₂ [17]. Also c.f. the list of materials displaying positive giant magnetoresistance (GMR) below, with the distinction between XMR and GMR being rather *arbitrary*. MR is defined as $(\rho(H) - \rho(0))/\rho(0)$, where $\rho(H)$ is the resistivity which increases in a magnetic field H . XMR is unusually high, reaching even values greater than 10^6 at low temperatures T of a few degrees Kelvin. E.g. XMR reaches 1.12×10^7 for $H = 33$ Tesla at $T=1.8$ K in PtBi₂ [17]. XMR does not *seem* to saturate with increasing H . Instead, it saturates below a small sample dependent characteristic T , and decays with increasing T , vanishing below room temperature. Further, it is *highly anisotropic* with respect to the direction of H , hence the Zeeman energy plays a minimum role, if any at all.

Our model in ref. [18] explains these features in principle. This model successfully explained positive GMR, which was observed in several materials, including Pt and Rh [19] (already in 1941), Sc [20], Tl₂Ba₂CuO_{6+ δ} [21], α -(BEDT-TTF)₂KHg(SCN)₄ [22]. After [18] was published, it was also observed in VO _{x} [23], Cd₃As₂ [24], YSb [25], ScPtBi [26], PtBi₂ [27], Cr₂NiGa [28], and Bi₂Te₃ [29]. All the recent XMR experiments bear a striking resemblance to these earlier GMR experiments. The main difference is the total magnitude of the effect.

Herein we develop further our model, by including additional microscopic processes via appropriate Feynman diagrams. In our approach the presence of weak disorder is assumed, necessarily including elastic spin scattering from spin-orbit and/or magnetic impurities.

In a metallic system, the dimensionless Hubbard interaction constant is $u = UN_F$, where U is the Hubbard constant and N_F the density of states at the Fermi level. Our mechanism is based on a *single band* picture, requiring that u be very close to a characteristic value u_0 (c.f. eq. (3) below). Most of the materials in which XMR occurs dispose more than one band intersecting the Fermi level. Hence it is assumed that u is very close to u_0 for *all* these bands.

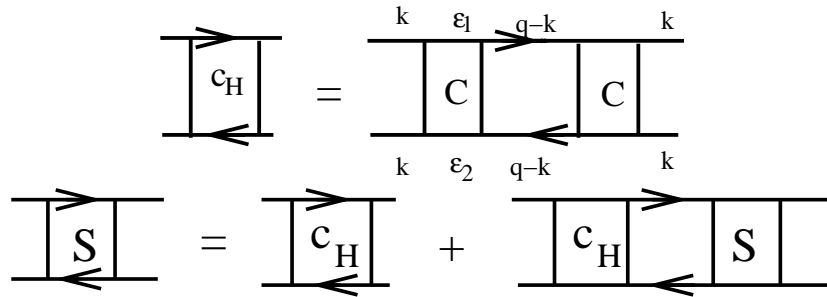


FIG. 1: Diagram for c_H given by eq. (4). In our model, the dominant dependence on the magnetic field H arises from c_H . The 2 cooperons are $C_{q,\omega}$ with $\omega = \epsilon_1 - \epsilon_2$. Also the ladder diagrams for S . In all diagrams, the simple horizontal lines stand for the Green's function G .

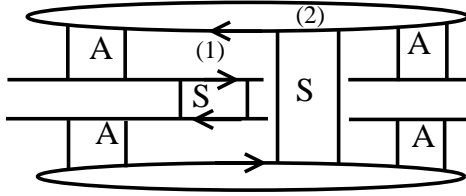


FIG. 2: Diagrams including the block J between pairs of propagators A^j - c.f. eq. (2) - in the upper and lower part of the diagram. We actually show the 3 different variants of these diagrams. J_1 corresponds to the case where propagator S marked (2) is absent, J_2 corresponds to the case where propagator S marked (1) is absent, and J_3 corresponds to both S 's being present. The A^j 's are *not* part of the contribution J , as they are considered separately in eq. (11) for Z_{2j} etc. These diagrams are part of the infinite series W_H in eq. (21).

As pointed out in [10], XMR is due to a small denominator $\rho(0)$ rather than a big numerator $\rho(H)$. This is consistent with our bulk mechanism. The conductivity $\sigma(H) = 1/\rho(H)$ is drastically enhanced for $H = 0$. As H increases, $\sigma(H)$ is quickly reduced, due to the decay of c_H in eq. (4), thus yielding the effect.

This paper is organized as follows. In section 2 we present the basis of our model. We introduce the particle-hole propagator $A^j(q, \omega)$, which includes both the Coulomb interaction and elastic spin scattering from the impurities. In section 3 we develop our basic formalism, which makes use of diagrams which are symmetric with respect to the main particle-hole line (which can be seen e.g. in diagrams 2,3). We also obtain the respective infinite series W_H . In section 4 we treat diagrams which are *non-symmetric*, but otherwise very similar to the ones of section 3. The respective infinite series X_H are also calculated. In section 5 we calculate the conductivity, based on a resummation of the series X_H and W_H . A physical interpretation of GMR/XMR as a manifestation of quantum interference effects at the macroscopic scale is also offered therein. In section 6 we consider an even more complete infinite set of diagrams, and we calculate, and plot, the respective conductivity. This section contains also the main discussion on the comparison with experiments. Section 7 is the Overview.

2. Basis of the model for GMR/XMR

The Green's function for the electrons is $G^{R,A}(k, \epsilon) = 1/(\epsilon - \epsilon_k + \epsilon_F \pm is)$, with $s = 1/2\tau$. ϵ_k is the dispersion relation, τ the momentum relaxation time due to impurities and ϵ_F the Fermi energy (which we take equal to the chemical potential). In the weak disorder regime $\epsilon_F\tau \gg 1$ [30].

In ref. [18] we introduced the propagators $A^j(q, \omega)$, $j = \pm 1, 0$, in the particle-hole spin-density channel. These obey the coupled Bethe-Salpeter equations $A^1 = U + U \mathcal{D}^1 A^1 + U \mathcal{D}^0 A^0$ and $A^0 = U \mathcal{D}^0 A^1 + U \mathcal{D}^{-1} A^0$. The components of the density and spin-density correlation functions are $\mathcal{D}^{\pm 1} = \mathcal{D}^{1, \pm 1}$, $\mathcal{D}^0 = \{\mathcal{D}^{0,0} - \mathcal{D}^{1,0}\}/2$ with $\mathcal{D}^{j,m}(q, \omega) = N_F \{Dq^2 + j4\tau_S^{-1}/3\} / \{Dq^2 + j4\tau_S^{-1}/3 - i\omega - im\omega_H\}$. Here q and ω are the momentum and energy difference between particle and hole lines, D the diffusion coefficient, ω_H the Zeeman energy and τ_S^{-1} the total elastic spin scattering rate due to impurities ($\hbar = c = 1$). $\tau^{-1} = \tau_0^{-1} + \tau_S^{-1}$, where τ_0^{-1} is the impurity scattering rate without spin-flip. (Also $A^{-1}(\omega_H) = A^1(-\omega_H)$.)

The solution of these equations is

$$A^j(q, \omega) = \frac{K_{uj} Dq^2 - iL_{uj} \omega + M_{uj}}{A_u Dq^2 - iB_u \omega + C_u}, \quad (1)$$

where in the "dynamic limit" $Dq^2 < \omega$ we have [18, 31]

$$A_u = 12 - 20u + 15u^2/2 + 6\Omega_H^2, \quad B_u = 4 - 6u + 3u^2/2 + 2\Omega_H^2, \quad C_u = r \{1 - 2u + 3u^2/4 + \Omega_H^2(1 - u^2/4)\}. \quad (2)$$

Here $r = 4\tau_S^{-1}/3$ and $\Omega_H = 3\omega_H\tau_S/4$. $M_{u0} = Uur(1 + \Omega_H^2)$, $M_{u1} = Ur(1 - u)$. In the following, we will assume that

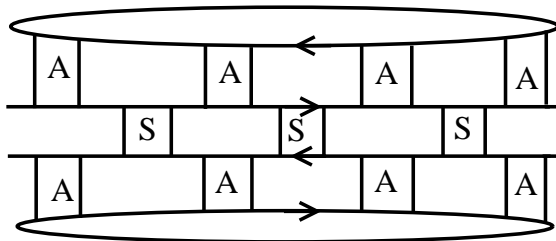


FIG. 3: Higher order diagram with $2 \times 2n = 8 A^j$'s, i.e. $n = 2$. To simplify the presentation, *only one propagator* S is shown between the A^j 's. In reality it is possible to have one or two S 's between the A^j 's, as in figure 2. All similar diagrams with up to $n = \infty$ are considered and summed up. These diagrams are part of the infinite series W_H in eq. (21).

the dependence on ω_H is *negligible*. For $\omega_H = 0$ we have

$$B_u = 0 \text{ for } u = u_0 = 0.845 . \quad (3)$$

We show below that this gives rise to an enhancement (“resonance”) factor proportional to $1/B_u$, c.f. eq. (12), which yields finally the extra-ordinary positive extreme magnetoresistance [18]. For metallic systems it is often appropriate to consider the effective RPA-corrected value $u_{eff} = u/(1 - u^2)$, which is to be compared to u_0 [18]. This u_{eff} was found in [18] to agree with u_0 for Sc, Pt and Rh, as calculated from first principles [32]. We also note that *no such enhancement* arises in the “static limit” $Dq^2 > \omega$.

$C(q, \omega) = 1/\{(2\pi N_F \tau^2)(Dq^2 - i\omega)\}$ is the cooperon propagator in the particle-particle channel [30, 33]. We consider the relevant contribution $c_H = \sum_q C^2(q, \omega = 0)$ - c.f. fig. 1. In $d = 3$ dimensions we have

$$c_H = \frac{1}{(2\pi)^3 N_F^2 \tau^4 \sqrt{D_i}} \sum_{n=0}^{\infty} \left\{ \frac{\sqrt{s}}{a_n^2} \frac{1}{a_n^2 + s} + \frac{1}{a_n^3} \tan^{-1} \left(\frac{\sqrt{s}}{a_n} \right) \right\} , \quad (4)$$

where $a_n^2 = 4D_{i\perp} eH(n + 1/2) + \tau_\phi^{-1}(T)$ [18, 33]. Here H is along the axis i and $i \perp$ stands for the plane perpendicular to the axis i . In our model, the dominant dependence on the magnetic field H arises from c_H . $\tau_\phi^{-1}(T) = \alpha + \beta T^p$ ($p \geq 1$) is the electron dephasing rate, which increases fast with T , thus leading to the decay of the cooperon, and yielding a *vanishing MR* (due to this mechanism) at higher T . We have shown [34] that $\alpha > (2/3)\tau_{sp}^{-1}$, where τ_{sp}^{-1} is the elastic scattering rate due to *magnetic* impurities only. We also overall assume $\tau_S^{-1} < \tau_\phi^{-1}(T)$. Note that external lines have momentum k , while in between the 2 cooperons they have $q - k$, where $q < 1/\sqrt{D\tau} \ll k_F$, with k_F the Fermi momentum. Note that the most relevant momentum range is $k \sim k_F$ for the Green's functions. Here $\Gamma(k, \epsilon_1, \epsilon_2) = G(k, \epsilon_1)G(k, \epsilon_2)$. We consider the respective infinite ladder series of c_H - c.f. fig. 1

$$S(k, \epsilon_1, \epsilon_2) = c_H \Gamma(k, \epsilon_1, \epsilon_2) \sum_{n=0}^{\infty} (c_H \Gamma^2(k, \epsilon_1, \epsilon_2))^n = \frac{c_H \Gamma(k, \epsilon_1, \epsilon_2)}{1 - c_H \Gamma^2(k, \epsilon_1, \epsilon_2)} . \quad (5)$$

Previously [18] we only considered the first term of this series. We have 3 contributions, from the respective diagrams shown in fig. 2.

$$J_1(k, \epsilon_1, \epsilon_2, \omega_1, \omega_2) = S(k, \epsilon_1, \epsilon_2) \Gamma^2(k, \epsilon_1, \epsilon_2) \Gamma(k, \epsilon_2 + \omega_2, \epsilon_1 - \omega_1) , \quad (6)$$

$$J_2(k, \epsilon_1, \epsilon_2, \omega_1, \omega_2) = S(k, \epsilon_2 + \omega_2, \epsilon_1 - \omega_1) \Gamma^2(k, \epsilon_2 + \omega_2, \epsilon_1 - \omega_1) \Gamma(k, \epsilon_1, \epsilon_2) , \quad (7)$$

$$J_3(k, \epsilon_1, \epsilon_2, \omega_1, \omega_2) = S(k, \epsilon_1, \epsilon_2) S(k, \epsilon_2 + \omega_2, \epsilon_1 - \omega_1) \Gamma^2(k, \epsilon_1, \epsilon_2) \Gamma^2(k, \epsilon_2 + \omega_2, \epsilon_1 - \omega_1) . \quad (8)$$

The total contribution equals $J(k, \epsilon_1, \epsilon_2, \omega_1, \omega_2) = J_1(k, \epsilon_1, \epsilon_2, \omega_1, \omega_2) + J_2(k, \epsilon_1, \epsilon_2, \omega_1, \omega_2) + J_3(k, \epsilon_1, \epsilon_2, \omega_1, \omega_2)$.

In sections 3 and 4 we account systematically for relevant diagrams containing the particle-hole propagator $A^j(q, \omega)$ and $J(k, \epsilon_1, \epsilon_2, \omega_1, \omega_2)$.

3. Symmetric in $A^j(q, \omega)$ diagrams

We consider appropriate diagrams, as in fig. 2. We show the calculation for 2 $A^j(q, \omega)$'s on the upper part of the diagram, and another 2 in the lower part. First, we will *only* consider diagrams with *mirror symmetric upper and lower parts*. Afterwards we will also consider diagrams which are *not mirror symmetric* with regards to the central particle-hole lines. The latter will turn out to be *sub-dominant*. Explicitly for fig. 2

$$w_{2j} = T^4 \sum_{q_1, \omega_1} (A^j(q_1, i\omega_1))^2 \sum_{q_2, \omega_2} (A^j(q_2, i\omega_2))^2 \sum_{k, \epsilon_1, \epsilon_2} J(k, i\epsilon_1, i\epsilon_2, i\omega_1, i\omega_2) . \quad (9)$$

Here ω_1, ω_2 and ϵ_1, ϵ_2 are Matsubara energies for bosons and fermions, respectively, and $\epsilon_1(\epsilon_1 - \omega_1) < 0$, $\epsilon_2(\epsilon_2 + \omega_2) < 0$. We first consider

$$F_2(i\omega_1) = T \sum_{\epsilon_1} J(k, i\epsilon_1, i\epsilon_2, i\omega_1, i\omega_2) = \frac{1}{2\pi i} \int_{-\infty}^{+\infty} d\epsilon (n_F(\epsilon) - n_F(\epsilon - i\omega_1)) J(k, \epsilon, i\epsilon_2, i\omega_1, i\omega_2) , \quad (10)$$

with $n_F(x) = (1/2)\tanh(x/2T)$ [35]. Then we carry out the summation

$$Z_{2j} = T \sum_{q_1, \omega_1} (A^j(q_1, i\omega_1))^2 F_2(i\omega_1) = \frac{1}{2\pi i} \int_{-\infty}^{+\infty} d\omega n_B(\omega) \sum_{q_1} (A^j(q_1, \omega))^2 F_2(\omega) \simeq \frac{s_j}{2\pi i} \int_{\omega_a}^{\omega_b} d\omega \frac{n_B(\omega) F_2(\omega)}{B_u \omega} , \quad (11)$$

where $n_B(x) = (1/2)\coth(x/2T)$ [35], $s_j = M_{uj}^2 \sqrt{|C_u|} / \{4\pi^2 (A_u D)^{3/2}\}$ for $d = 3$, and $\omega_a < \omega_b$ are both of the order of a fraction of ϵ_F . Use was made of the equality

$$z_{2n} = \int_{x_0 - \delta}^{x_0 + \delta} \frac{f(x) dx}{(x - x_0 - i\delta)^{2n}} \simeq \frac{g_n f(x_0)}{(2n - 1) 2^{n-1} \delta^{2n-1}} , \quad (12)$$

with $|g_n| = 1$ [36], $\delta = B_u \omega \rightarrow 0$ for $u \rightarrow u_0$, $x = A_u D q^2$, and $x_0 = -C_u > 0$. The summations over q_2, ω_2 proceed in the same way.

Finally, with $\omega_0 = \omega_b - \omega_a$ and considering $n_F(\epsilon) - n_F(\epsilon - \omega) \simeq \omega \partial n_F(\epsilon) / \partial \epsilon$ ($T \rightarrow 0$) we obtain

$$Z_{2j} = \frac{s_j \omega_0}{4\pi^2 B_u} J(k, \epsilon = 0^+, i\epsilon_2, 0, i\omega_2) . \quad (13)$$

Carrying out the summations over q_2, ω_2 and ϵ_2 yields

$$w_{2j} = \left(\frac{s_j \omega_0}{4\pi^2 B_u} \right)^2 \sum_k J(k, \epsilon = 0^+, \epsilon = 0^-, 0, 0) . \quad (14)$$

We want to evaluate $P = \sum_{k < k_F} J(k, 0^+, 0^-, 0, 0) = 2h_a + h_b$, with the contributions $2h_a$ (due to $J_1 + J_2$) and h_b (due to J_3). Now we take $S_k = S(k, \epsilon = 0^+, \epsilon = 0^-)$ and $\Gamma_k = \Gamma(k, \epsilon = 0^+, \epsilon = 0^-)$. With

$$X_k = (\epsilon_k - \epsilon_F)^2 + s^2 , \quad (15)$$

we have

$$h_a = \sum_{k < k_F} S_k \Gamma_k^3 = \sum_{k < k_F} \frac{c_H}{X_k^2 - c_H} \frac{1}{X_k^2} , \quad h_b = \sum_{k < k_F} S_k^2 \Gamma_k^4 = \sum_{k < k_F} \frac{c_H^2}{(X_k^2 - c_H)^2} \frac{1}{X_k^2} . \quad (16)$$

We take $\sum_{k < k_F} = N_F \int_0^{\epsilon_F} d\epsilon_k$. Then the two integrals can be calculated exactly using a symbolic manipulation package. We use Mathematica throughout. With $r_{\pm} = \sqrt{s^2 \pm \sqrt{c_H}}$, the total result is

$$P = N_F \left\{ \frac{2}{\sqrt{c_H}} \left[\frac{1}{r_-} \tan^{-1} \left(\frac{\epsilon_F}{r_-} \right) - \frac{1}{r_+} \tan^{-1} \left(\frac{\epsilon_F}{r_+} \right) \right] + \frac{7\sqrt{c_H} + 6s^2}{8r_+^3 \sqrt{c_H}} \tan^{-1} \left(\frac{\epsilon_F}{r_+} \right) \right. \\ \left. + \frac{7\sqrt{c_H} - 6s^2}{8r_-^3 \sqrt{c_H}} \tan^{-1} \left(\frac{\epsilon_F}{r_-} \right) + \frac{1}{4} \frac{\epsilon_F}{c_H - s^4} \frac{c_H + s^2(s^2 + \epsilon_F^2)}{c_H - (s^2 + \epsilon_F^2)^2} - \frac{\epsilon_F}{2s^2} \frac{1}{s^2 + \epsilon_F^2} - \frac{1}{2s^3} \tan^{-1} \left(\frac{\epsilon_F}{s} \right) \right\} . \quad (17)$$

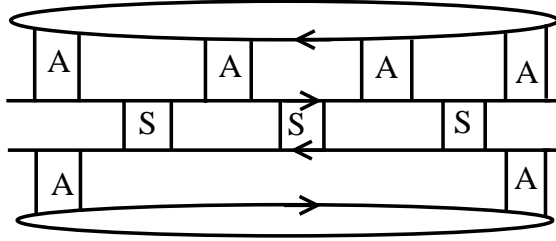


FIG. 4: Non-symmetric diagram. Here two A^j 's are missing below the main particle-hole lines. The outermost A^j 's are always kept in such diagrams. As in fig. 3, to simplify the presentation, only one propagator S is shown between the A^j 's. In reality it is possible to have one or two S 's between the A^j 's, as in figure 2. This diagram is part of the infinite series $X_2(z)$ in eq. (25).

For higher orders $n > 1$, as in fig. 3, it is easy to show that the respective result is $w_{2n,j} = r_0 M_{u,j}^{4n} P^{2n-1} / \{2^{2n-2} (2n-1)^2 B_u^{4n-2}\}$, with $r_0 = \omega_0^2 |C_u| / \{16\pi^4 (A_u D)^3\}$.

Now, the ratio $\Lambda_u = M_{u0}/M_{u1} = \sqrt{s_0/s_1}$ equals 5.45 and 4.07 for $u = u_0$ and $0.95 u_0$, respectively. It is easy to consider all diagrams which contain factors of the type $\{(A^0(q, \omega))^4 + (A^1(q, \omega))^4\}^n$ for any $n \geq 1$. For this purpose we consider the factor (in which the numerator of $A^j(q, \omega)$ is approximated by M_{uj})

$$l_0^4 = M_{u0}^4 (1 + 1/\Lambda_u^4) . \quad (18)$$

Considering $\Lambda_u = 5$, $1/\Lambda_u^4 = 1/625$ is a small number. Then, with w_{2n} containing the contributions from all these diagrams, we have the series [37]

$$W_{1H} = \sum_{n=1}^{\infty} w_{2n} = 2r_0 \sum_{n=1}^{\infty} \frac{P^{2n-1} l_0^{4n}}{2^{2n} (2n-1)^2 B_u^{4n-2}} = r_0 l_0^2 z I_1(z)$$

$$I_1(z) = \sum_{m=0}^{\infty} \frac{z^{2m}}{(m+1/2)^2} , \quad z = P l_0^2 / (2 B_u^2) . \quad (19)$$

We also consider the rest of the diagrams of order $1/\Lambda_u^4$. Because there are $4 \times 3^{n-2}$ such terms for $n > 1$ (with $2n-1 = 3, 5, 7, \dots$ etc. blocks P from eq. (17)), we obtain the series

$$W_{2H} = 8r_0 l_0^2 z^3 I_2(z) , \quad I_2(z) = \sum_{n=0}^{\infty} \frac{3^n z^{2n}}{(n+3/2)^2} . \quad (20)$$

The total contribution due to W_{1H} and W_{2H} is

$$W_H = W_{1H} + W_{2H}/\Lambda_u^4 + O(1/\Lambda_u^8) . \quad (21)$$

We also write this as

$$W_H = r_0 l_0^2 z I(z) , \quad I(z) = I_1(z) + 8z^2 I_2(z)/\Lambda_u^4 . \quad (22)$$

4. Non-symmetric in $A^j(q, \omega)$ diagrams

Now we turn our attention to the non-symmetric diagrams (with regards to the central particle-hole lines). These are of the same type as the ones considered above, but with a distinct difference. There are two $A^j(q, \omega)$'s missing either in the upper or in the lower part of the diagrams as in figs. 4 and 5. In particular, we consider diagrams such that the leftmost and rightmost $A^j(q, \omega)$'s are kept in place. The two missing $A^j(q, \omega)$'s would be located anywhere

in between these two external ones. Also, due to this deletion, two energy summations are removed as well, which yields an overall factor $i^2 = -1$ for these non-symmetric diagrams - c.f. $X_1(z)$ and $X_2(z)$ below.

The calculation here proceeds in a very similar manner as for the symmetric diagrams. Of course care has to be taken with all the factors which appear in an upper-lower non-symmetric way. E.g. all the diagrams here contain the asymmetry factor $h_m = g_m g_{m-1} = (-1)^{m+1}$ [36]. The diagrams herein contain the factors Q_1 and Q_2 shown in figs. 6 and 7 respectively. We have

$$Q_1 = \sum_{k < k_F} \{4 S_k^2 \Gamma_k^5 + 4 S_k^3 \Gamma_k^6 + S_k^4 \Gamma_k^7\} , \quad (23)$$

and

$$Q_2 = \sum_{k < k_F} \{8 S_k^3 \Gamma_k^7 + 12 S_k^4 \Gamma_k^8 + 6 S_k^5 \Gamma_k^9 + S_k^6 \Gamma_k^{10}\} . \quad (24)$$

Assuming a constant density of states N_F , these integrals can be calculated exactly, as we did for P above.

The total contribution from the infinite series here is

$$X_H = X_1(z) + X_2(z) , \quad (25)$$

where $X_2(z) = -c_0 Q_2 f_2(z)$, with $(2m - 3)$ terms of order z^{2m-4} , and

$$f_2(z) = \sum_{m=2}^{\infty} \frac{h_m z^{2m}}{2m-1} = -z^2 + z \tan^{-1}(z) . \quad (26)$$

Also $X_1(z) = -d_0 Q_1^2 f_1(z)$, with $(2m^2 - 7m + 6)$ terms of order z^{2m-5} and

$$f_1(z) = \sum_{m=3}^{\infty} \frac{h_m (2m^2 - 7m + 6) z^{2m}}{(2m-1)(2m-3)} = \frac{1}{2(1+z^2)} \{3z^2 + 2z^4 - 3(z+z^3) \tan^{-1}(z)\} , \quad (27)$$

where $c_0 = 8r_0 B_u^4/P^4 l_0^2$ and $d_0 = c_0/P$. In the limit $z \rightarrow \infty$ these functions are $f_1(z) \simeq z^2$ and $f_2(z) \simeq -z^2$.

Now we will examine closely some particular limits for X_H . First, for $\epsilon_F \tau \gg 1$ we may expand in powers of c_H ($c_H \propto \tau^{-4} \propto s^4$). Here we explicitly consider that $s^2 > \sqrt{c_H}$. The specific case $s^2 \geq \sqrt{c_H}$ is treated below. So we have $S(k) = c_H \Gamma_k + O(c_H^2)$ and

$$Q_1 = r_1 c_H^2 + O(c_H^3) , \quad Q_2 = r_2 c_H^3 + O(c_H^4) , \quad P = P_0 c_H + O(c_H^2) . \quad (28)$$

Here $r_1 = 4 \sum_{k < k_F} X_k^{-7} = (231/512)(N_F \pi/s^{13})$, $r_2 = 8 \sum_{k < k_F} X_k^{-10} = (12155/16384)(N_F \pi/s^{19})$, $P_0 = 2 \sum_{k < k_F} X_k^{-4} = (5/16)(N_F \pi/s^7)$.

Using these in the limit $z \rightarrow \infty$ we have

$$X_H \simeq (c_0 Q_2 - d_0 Q_1^2) z^2 = \frac{2r_0 l_0^2 y_0 c_H}{P_0^3} , \quad (29)$$

with $y_0 = P_0 r_2 - r_1^2 = \{(3707/20480) \simeq 0.1810\} (N_F^2 \pi^2/4s^{26})$.

We note that in this limit X_H in eq. (29) is *independent* of B_u . This is due to the combination $X_H \propto z^2 B_u^4$. The same applies for X_H in eq. (34) below.

Next, we write $x_1 = s^2 - \sqrt{c_H}$ and $x_2 = s^2 + \sqrt{c_H}$, and we consider the limit

$$x_1 \rightarrow 0^+ , \quad (30)$$

i.e. c_H is allowed to approach s^4 from below. As c_H is a decreasing function of H and T , this condition may only apply for small H and low T , i.e. in the region of the phase diagram where the magnitude of the conductivity is *maximum*.

Then, with $g = (\epsilon_F^2 + s^2)^2 - c_H$, we obtain the limiting forms

$$P = \frac{p_{1A}}{x_1^{3/2}} + \frac{p_{1B}}{x_1 x_2} + O(1/\sqrt{x_1}) , \quad (31)$$

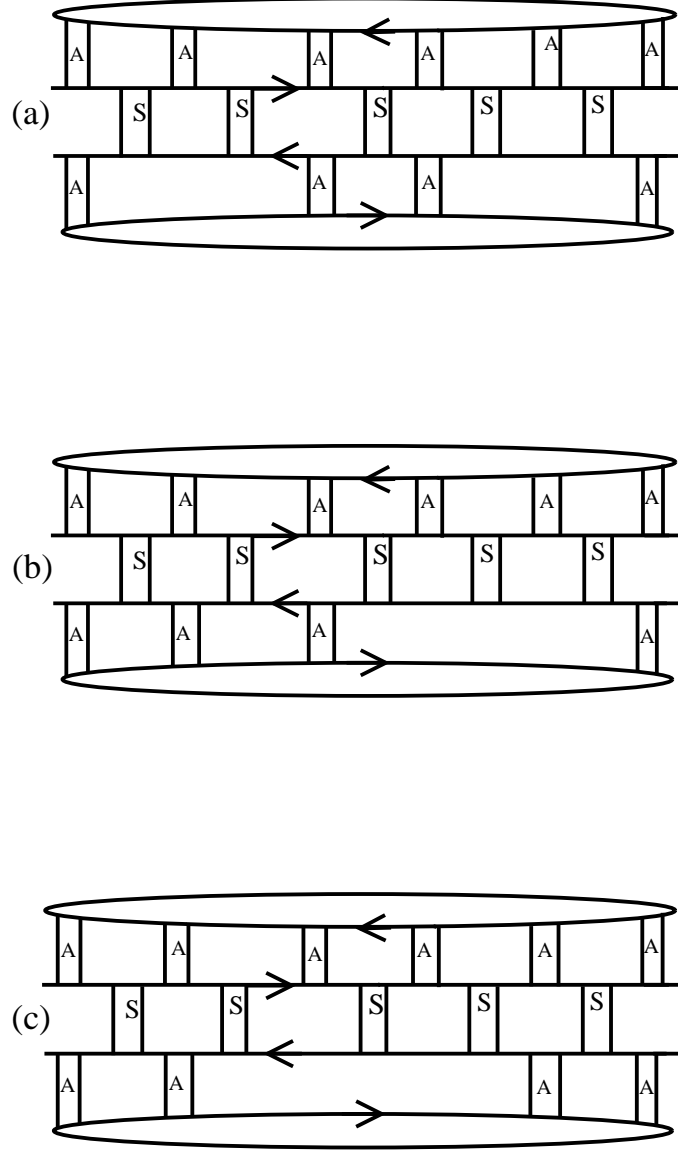


FIG. 5: Non-symmetric diagrams. Two A^j 's are missing below the main particle-hole lines. Note that fig. (a), (b), and (c) differ in the positions of missing A^j 's. All these diagrams with $2m + 2(m - 1) = 4m - 2$ A^j 's are taken into account with up to $m = \infty$. Diagrams (a) are part of the infinite series $X_1(z)$ in eq. (25), while diagrams (b) and (c) are part of the infinite series $X_2(z)$ in eq. (25).

with $p_{1A} = N_F \left(c_H^{1/2} - 6x_1 \right) \tan^{-1} \left(\epsilon_F / \sqrt{x_1} \right) / \left\{ 8 c_H^{1/2} \right\}$, $p_{1B} = N_F \epsilon_F \left[c_H + s^2 (s^2 + \epsilon_F^2) \right] / \{ 4g \}$,

$$Q_1 = \frac{q_{1A}}{x_1^{7/2}} + \frac{q_{1B}}{x_1^3 x_2^3} + O(x_1^{-5/2}) , \quad (32)$$

with $q_{1A} = N_F \left\{ -512 s^6 + 1652 s^4 c_H^{1/2} - 1798 s^2 c_H + 663 c_H^{3/2} \right\} \tan^{-1} \left(\epsilon_F / \sqrt{x_1} \right) / \{ 256 c_H \}$, $q_{1B} =$

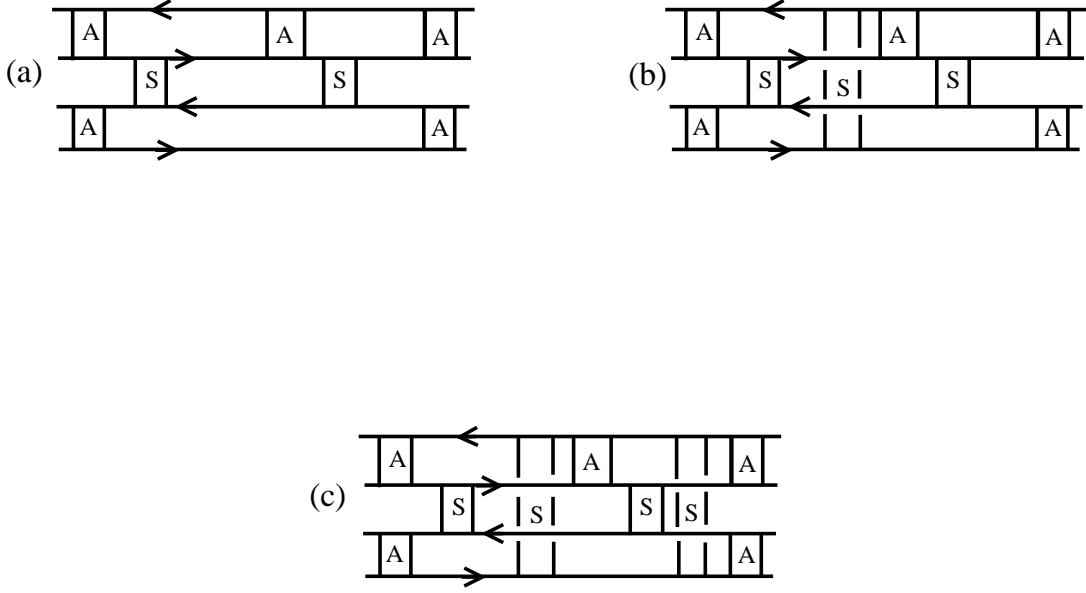


FIG. 6: Diagrams for the *internal* part Q_1 , i.e. without the outer bubble lines. Three distinct contributions (a)-(c) are shown. All blocks S are explicitly shown. The multiplicity prefactors due to the different positions of S 's, c.f. eq. (23), are equal to 4 for (a), 4 for (b) and 1 for (c). The A^j 's are *not* included in Q_1 , only the G 's and S 's.

$N_F \epsilon_F [6s^8(91s^2 + 43\epsilon_F^2) - 7c_H(196s^6 + 93s^4 \epsilon_F^2) + c_H^2(946s^2 + 453\epsilon_F^2)] / \{384 g\}$, and

$$Q_2 = \frac{q_{2A}}{x_1^6 x_2^5} + \frac{q_{2B}}{x_1^5 x_2^{11/2}} + \frac{q_{2C}}{x_1^5 x_2^5} + O(x_1^{-4}) , \quad (33)$$

with $q_{2A} = N_F \left\{ -96096 s^{20} + 23472 s^{18} c_H^{1/2} + 496464 s^{16} c_H - 106684 s^{14} c_H^{3/2} - 1033822 s^{12} c_H^2 + 186043 s^{10} c_H^{5/2} + 1088757 s^8 c_H^3 - 149086 s^6 c_H^{7/2} - 584084 s^4 c_H^4 + 47263 s^2 c_H^{9/2} + 129789 c_H^5 \right\} \tan^{-1}(\epsilon_F/\sqrt{x_1}) / \{16384 c_H^{3/2}\}$,
 $q_{2B} = N_F \left\{ 96096 s^{20} + 23472 s^{18} c_H^{1/2} - 496464 s^{16} c_H - 106684 s^{14} c_H^{3/2} + 1033822 s^{12} c_H^2 + 186043 s^{10} c_H^{5/2} - 1088757 s^8 c_H^3 - 149086 s^6 c_H^{7/2} + 584084 s^4 c_H^4 + 47263 s^2 c_H^{9/2} - 129789 c_H^5 \right\} \tan^{-1}(\epsilon_F/\sqrt{x_2}) / \{16384 c_H^{3/2}\}$, and
 $q_{2C} = N_F \left\{ \epsilon_F (80637 c_H^5 - 102009 s^4 c_H^4 - 148193 s^8 c_H^3 + 387913 s^{12} c_H^2 - 282716 s^{16} c_H + 70416 s^{20}) + \epsilon_F^3 (141789 s^2 c_H^4 - 447258 s^6 c_H^3 + 558129 s^{10} c_H^2 - 320052 s^{14} c_H + 70416 s^{18}) \right\} / \{24576 c_H g\}$.

Now, taking $c_H \simeq s^4$ in x_2 and g , but *not* in x_1 , and $\epsilon_{F\tau} \gg 1$ yields $p_{1A} = N_F \pi / 16$, $q_{1A} = -15 N_F \pi s^2 / 1536$ and $q_{2A} = 63 N_F \pi s^4 / 32768$. Then the leading contribution in $1/x_1$ is

$$X_H = \frac{2r_0 l_0^2}{p_{1A}^2} \frac{F_1}{x_1^{5/2}} , \quad F_1 = q_{2A} - q_{1A}^2 / p_{1A} = \frac{77\pi N_F}{32768} . \quad (34)$$

Comparison between the series W_H and X_H .

The z^{2m} term of the series X_H dominates over the respective term of the series W_H . The reason is the high value of the numerical prefactor at any high enough power z^{2m} , which *overcompensates* the missing factor $1/B_u^2$ from the two missing A^j 's. For the limit $x_1 \rightarrow 0$ this is seen e.g. in the ratio

$$(X_{2,m}/W_{1H,m}) = 8B_u^2 q_{1a}^2 (2m-1)(2m^2-7m+6) / \{N_F^2 p_{1a}^4 l_0^2 (2m-3) x_1\} . \quad (35)$$

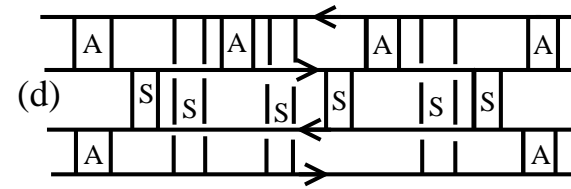
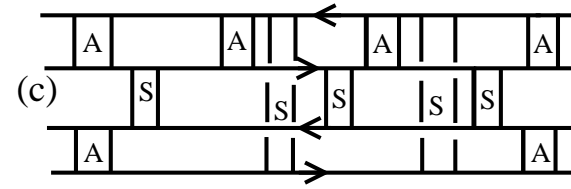
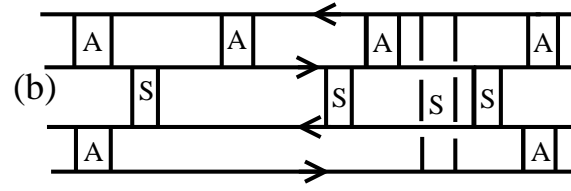
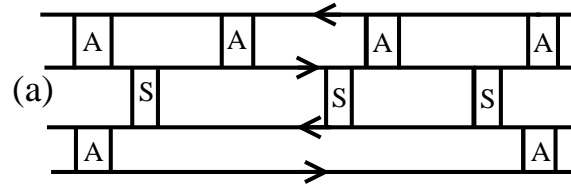


FIG. 7: Diagrams for the *internal* part Q_2 , i.e. without the outer bubble lines. Four distinct contributions (a)-(d) are shown.

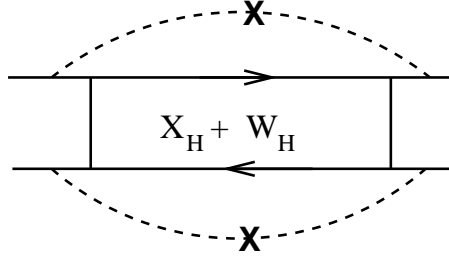


FIG. 8: Diagrams for A_H in eq. (38) and B_H in eq. (37). The dashed external lines with the cross stand for *impurity scattering*. B_H corresponds to the case of one such scattering line, either above or below the central box, and also to the *absence* of these lines. A_H corresponds to the presence of *both* scattering lines.

Here the factor $1/x_1$ contributes as well. The ratio $(X_{1,m}/W_{1H,m})$ behaves similarly. For *finite* x_1 and $\epsilon_F \tau \gg 1$ - c.f. eq. (28) - the ratio is

$$(X_{2,m}/W_{1H,m}) = 8r_1^2 B_u^2 (2m-1)(2m^2-7m+6) / \{P_0^4 l_0^2 (2m-3)\} , \quad (36)$$

and similarly for the ratio $(X_{1,m}/W_{1H,m})$.

However, the sign of the terms of the series X_H *alternates* with m as $h_m = (-1)^{m+1}$. As a result, X_H cannot dominate over W_H , and W_H makes the main contribution. Moreover, as shown above, for large z the X_H contribution is limited in magnitude, as opposed to the W_H contribution. For completeness, we include both W_H and X_H in A_H and B_H below.

5. Calculation of the conductivity using the series W_H and X_H

With these series at hand, we further consider three types of diagrams incorporating them. The ones with a single external impurity scattering line and the ones *without* such a line - c.f. fig. 8 - yield a *combined* contribution $B_H G_R(k, \epsilon) G_A(k, \epsilon)$, where

$$B_H = (W_H + X_H) \left(1 + \frac{\epsilon_F}{\pi s}\right) . \quad (37)$$

The diagrams with two external impurity scattering lines - c.f. fig. 8 - yield a contribution A_H with

$$A_H = (W_H + X_H) / (4\pi^2 s^2) . \quad (38)$$

Hence in total we have

$$\Gamma_H = A_H + B_H G_R(k, \epsilon) G_A(k, \epsilon) . \quad (39)$$

Now we consider the total conductivity as

$$\sigma = \sigma_D + \sigma_A(H) , \quad (40)$$

where, σ_D is the Drude term, and for $T \rightarrow 0$, $\sigma_A(H)$ is given by

$$\sigma_A(H) = \frac{e^2}{3\pi m^2} \int_0^{k_F} d\vec{k} k^2 \{G_R(k, 0) G_A(k, 0)\}^2 \Gamma_H . \quad (41)$$

Calculating the integral we obtain

$$\sigma_A(H) = \frac{e^2 N_F}{3\pi m} \left\{ \frac{\epsilon_F}{8s^5} (4 A_H s^2 + 3 B_H) \tan^{-1} \left(\frac{\epsilon_F}{s} \right) - \frac{B_N}{4s^4} + \frac{5 B_H}{8 s^2 (s^2 + \epsilon_F^2)} \right\} . \quad (42)$$

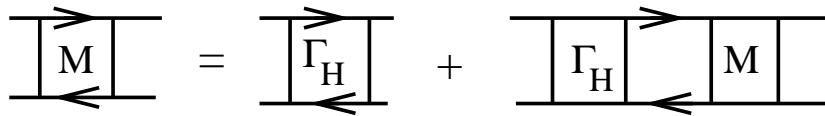


FIG. 9: Ladder diagrams for the block M in terms of Γ_H .



FIG. 10: Conductivity diagram for eq. (48). A block M in the middle, and current vertices on each side.

Considering the term W_H *only* in the low disorder limit $\epsilon_F \tau \gg 1$, we notice that $\sigma_A(H)$ is

$$\sigma_A(H) = s_0 f(z) \quad (43)$$

with, c.f. eqs. (19),

$$f(z) = z I_1(z) \quad , \quad (44)$$

and

$$s_0 = \frac{e^2 N_F \epsilon_F^2 r_0 l_0^2}{16 m s^6} \quad . \quad (45)$$

Here $l_0 = r m_u \lambda$, $\lambda^4 = 1 + 1/\Lambda_u^4$, $r = 4/(3 \tau_S) = b_1 s$ with $b_1 = O(1)$, $M_{u0} = r m_u$, $m_u = Uu$, $C_u = r c_u$. The Drude term is

$$\sigma_D = \frac{e^2}{3\pi m^2} \int_0^{k_F} d\vec{k} k^2 G_R(k, 0) G_A(k, 0) \simeq \frac{e^2 N_F \epsilon_F}{3\pi m s} \tan^{-1} \left(\frac{\epsilon_F}{s} \right) \quad . \quad (46)$$

It turns out that eq. (43) has very interesting properties, relevant to the XMR experiments. For intermediate magnetic fields H it yields XMR proportional to H^b , $b \geq 1$. For higher H the behavior changes with $b \rightarrow 2$ as H grows. This is how the variety of the values of the exponent b observed experimentally can be explained.

Then we consider the infinite ladder sum of Γ_H - c.f. fig. 9

$$M(k, \epsilon) = \frac{\Gamma_H}{1 - \Gamma_H G_R(k, \epsilon) G_A(k, \epsilon)} \quad . \quad (47)$$

For $T \rightarrow 0$ the total conductivity due to this mechanism is given by

$$\sigma_M = \frac{e^2}{3\pi m^2} \int_0^{k_F} d\vec{k} k^2 \{G_R(k, 0) G_A(k, 0)\}^2 M(k, 0) = -\sigma_D + \sigma_C(H) \quad . \quad (48)$$

Eq. (48) is a Baym-Kadanoff conserving approximation [38],[18],[31]. This is seen by considering the free energy diagrams which result by removing the two current vertices from the conductivity diagrams above. It turns out then that the only way to reintroduce the current vertices and obtain an *enhanced* conductivity yields precisely the original diagrams. $(-\sigma_D)$ is *minus* the well known Drude term. This results from Γ_H in the denominator of $M(k, \epsilon)$, and its origin is more clearly seen by considering the limit $\Gamma_H \rightarrow \infty$ in eq. (48). As a result, the Drude term *drops out* of the total conductivity $\sigma(H)$, which is given by the highly H -sensitive term $\sigma_C(H)$. In turn, this is how giant magnetoresistance appears as a *bulk effect* in these systems, as $\sigma_C(H)$ decreases quickly with increasing H . This is yet another impressive manifestation of quantum interference effects at the macroscopic scale. The cooperon incorporates the effects of counter-propagating electron paths [30], which interfere destructively with the increasing magnetic flux enclosed (due to H). The present mechanism acts as a 'lense', which drastically magnifies the interference effects.

We have

$$\sigma(H) = \sigma_D + \sigma_M = \sigma_C(H) \quad , \quad (49)$$

$$\sigma_C(H) = \frac{2e^2 N_F}{3\pi m S_H} \left\{ \frac{\epsilon_F Y_+}{R_+} \tan^{-1} \left(\frac{\epsilon_F}{R_+} \right) - \frac{\epsilon_F Y_-}{R_-} \tan^{-1} \left(\frac{\epsilon_F}{R_-} \right) + Y_+ \ln \left(\frac{R_+^2}{R_+^2 + \epsilon_F^2} \right) - Y_- \ln \left(\frac{R_-^2}{R_-^2 + \epsilon_F^2} \right) \right\} \quad , \quad (50)$$

$$R_{\pm} = \sqrt{s^2 - Y_{\pm}} \quad , \quad Y_{\pm} = (A_H \pm S_H)/2 \quad , \quad S_H = \sqrt{A_H^2 + 4B_H} \quad . \quad (51)$$

Here we assumed a constant N_F , and the ln terms are much smaller than the first terms and may be omitted.

This relation yields GMR as a function of H with $\rho(H) = 1/\sigma(H)$. The magnitude of GMR increases with the weakening of disorder, i.e. for increasing $\epsilon_F \tau$. From eq. (50), GMR can be attributed to $R_+(H=0) \rightarrow 0^+$, i.e. $Y_+(H=0) \rightarrow s^2$, so that a substantial contribution comes from $1/R_+$. As H increases, c_H is reduced, and so are the series X_H and W_H , yielding a lower $\sigma(H > 0)$.

We defer a further discussion on GMR to the end of section 6, after eq. (60).

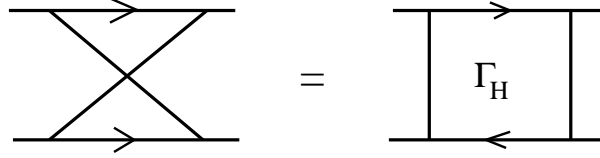


FIG. 11: The 'bow-tie' shaped Γ_H . It is derived from Γ_H just by rotating around the lower line. Notice the sense of the arrows shown.

6. More complicated diagram series and the respective conductivity

In this section we introduce additional diagrammatic contributions, which include the block Γ_H in *more complicated* series than in the previous section.

First, we introduce the 'bow-tie' shaped Γ_H , shown in fig. 11. It is derived from Γ_H just by rotating around the lower line. Then, we form a new effective interaction by combining two or more such bow-tie Γ_H 's in series, as shown in fig. 12. We draw attention to the precise direction of arrows in the figure. We note that the term with only one Γ_H is already contained in the series for M as in eq. (47). Explicitly we have (with Γ_k defined right before eq. (5))

$$R(k) = \Gamma_H^2 \Gamma_k \sum_{m=0}^{\infty} (\Gamma_H \Gamma_k)^m = \frac{\Gamma_H^2 \Gamma_k}{1 - \Gamma_H \Gamma_k} \quad . \quad (52)$$

Subsequently we will form ladder diagrams which include both $R(k)$'s and M 's. These are split into two discrete contributions L_1 and L_2 obeying the coupled Bethe-Salpeter equations in fig. 13

$$L_1 = \Gamma_H + \Gamma_H \Gamma_k L_1 + R(k) \Gamma_k L_2 + L_2 \Gamma_k R(k) \quad , \quad (53)$$

$$L_2 = R(k) + R(k) \Gamma_k L_1 + L_1 \Gamma_k R(k) + \Gamma_H \Gamma_k L_2 + L_2 \Gamma_k \Gamma_H \quad . \quad (54)$$

We note that without the terms $R \Gamma_k L_2$ eq. (53) yields precisely $L_1 = M(k, \epsilon)$.

The contributions to the conductivity from L_1 and L_2 are shown in fig. 14. Taking

$$L(k) = L_1 + L_2 \quad , \quad (55)$$

these two diagrams can be combined into a single expression. For $T \rightarrow 0$ the total contribution from $L(k)$ is given by

$$\sigma_L = \frac{e^2}{3\pi m^2} \int_0^{k_F} d\vec{k} k^2 \{G_R(k, 0)G_A(k, 0)\}^2 L(k) \quad . \quad (56)$$

We also subtract relevant contributions to avoid double counting. Again this is a Baym-Kadanoff conserving approximation, like the equivalent eq. (48). Calculating the integral, with the assumption of a constant N_F , we obtain

$$\sigma_L = -\sigma_D + \sigma_*(H) \quad , \quad (57)$$

where

$$\sigma_*(H) = \frac{e^2 N_F \epsilon_F A_*}{3\pi m T_H} \left\{ \frac{K_+}{V_+} \tan^{-1} \left(\frac{\sqrt{2} \epsilon_F}{V_+} \right) - \frac{K_-}{V_-} \tan^{-1} \left(\frac{\sqrt{2} \epsilon_F}{V_-} \right) \right\} \quad . \quad (58)$$

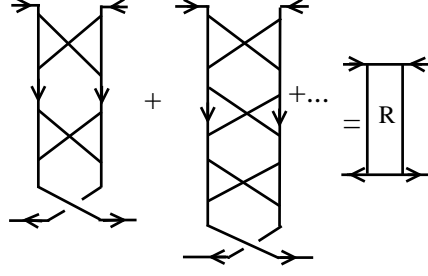


FIG. 12: Diagrams for the block $R(k)$ in eq. (52). We sum up the infinite series which starts with two 'bow-tie' shaped Γ_H 's - c.f. fig. 11. The term with only one Γ_H is already contained in the series for M as in eq. (47). Notice the sense of the arrows.

$$\begin{aligned}
 \overleftrightarrow{L_1} &= \overleftrightarrow{\Gamma_H} + \overleftrightarrow{\Gamma_H} \overleftrightarrow{\Gamma} \overleftrightarrow{L_1} + \overleftrightarrow{R} \overleftrightarrow{\Gamma} \overleftrightarrow{L_2} \\
 \overleftrightarrow{L_2} &= \overleftrightarrow{R} + \overleftrightarrow{R} \overleftrightarrow{\Gamma} \overleftrightarrow{L_1} + \overleftrightarrow{\Gamma_H} \overleftrightarrow{\Gamma} \overleftrightarrow{L_2}
 \end{aligned}$$

FIG. 13: Coupled equations for the propagators L_1 and L_2 . We do *not* show the full, i.e. mirror-symmetric, terms, omitting $L_2 \Gamma_k R$, $L_1 \Gamma_k R$, and $L_2 \Gamma_k \Gamma_H$. Notice the *precise sense* of the arrows.

Here $A_* = (c_*^2 - 3 + c_* - 1/c_*) / \{\sqrt{2} (c_* - d_*) [(a_* - c_*)^2 + b_*^2]\} = 0.401872$. The constants arise as solutions of a quartic equation, and are given by $c_* = 2.748403$, $a_* = 1.234465$, $b_* = 1.350696$, $d_* = -0.2173337$. Also $V_{\pm} = \sqrt{2s^2 - \sqrt{c_*} K_{\pm}}$, $K_{\pm} = \sqrt{c_*} A_H \pm T_H$, $T_H = \sqrt{c_* A_H^2 + 4B_H}$. There are also ln terms, which are much smaller than the terms shown, and may be omitted.

GMR is obtained when $\sigma_*(H \rightarrow 0)$ is significantly enhanced. This is the case especially for

$$V_+^2 = 2s^2 - \sqrt{c_*} K_+ \rightarrow 0 . \quad (59)$$

Using eqs. (38) and (37), this happens for

$$W_H + X_H = \frac{s^4}{c_*} \frac{1}{\epsilon_F / (\pi s) + 1 + 1/(4\pi^2)} = w_* . \quad (60)$$

We note here that the equivalent relation $R_{\pm}^2 \rightarrow 0$ in the previous section yields $W_H + X_H = c_* w_*$. I.e. the consideration of all these additional diagrams in the present section *reduced* the appropriate value of $W_H + X_H$, required for GMR, by a factor of c_* .

As for eq. (50), $\sigma(H)$ is a decreasing function of H due to the decay of c_H with H . This yields *positive* MR. Further, we see that the cleaner the sample, i.e. the higher the ratio ϵ_F/s is, the smaller w_* is. Also $w_* \propto s^4$. Together these

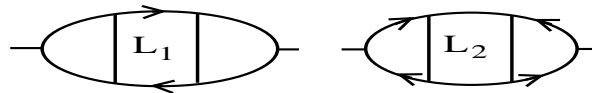


FIG. 14: Conductivity diagrams for the two propagators L_1 and L_2 .

facts imply that *the magnitude of GMR is higher in cleaner samples, in agreement with experiments* [8]. This also implies that in cleaner samples the conditions, due to small values of B_u and otherwise as elaborated upon in eqs. (29) and (34) in Section 4, are easier to satisfy, making GMR more likely to appear therein.

The discussion about the H^b dependence of XMR, given after eq. (46), applies here as well. The anisotropy, seen in the experiments, with the direction of the H is easily explained in terms of the anisotropic diffusion coefficient entering in c_H . The main T dependence comes from the fast rise of $\tau_\phi^{-1}(T)$ with T , which yields the respective decay of GMR.

PtBi₂ deserves a special mention. Pt was shown experimentally in [19] to display GMR, in accordance with the value of u for (fcc) Pt following our theory [18]. Interestingly, PtBi₂ in ref. [17] has the crystal structure of (fcc) Pt with an additional Bi matrix. The samples in [17] display possibly the biggest XMR found, as mentioned in the first paragraph of the Introduction.

Moreover, we draw attention to the fact that XMR and GMR have appeared in a number of compounds which contain Pt and/or Sc, both of which are expected to display these effects [18]. These are PtBi₂ [17] and PtSn₄ [1] for XMR, and ScPtBi [26] and PtBi₂ [27] for GMR. Together with the data from Rh [19], this set of data supports our theoretical model.

We plot the conductivity from our eqs. (57),(58) in fig. 15. $\sigma_*(H)$ can be much bigger than the Drude term σ_D . The resistivity eventually saturates at some high value of the field H . σ_* decreases with H until it becomes smaller than σ_D , at which point saturation is reached. For similar reasons the resistivity should actually saturate at high enough H in all cases.

In order to consider z values bigger than 1, which arise, say, from $B_u \rightarrow 0$, we need a reasonable estimator for W_H , i.e. $I(z)$ (and likewise for X_H). $I(z)$ was calculated to infinite order from Feynman diagrams, and, physically speaking, should *converge* for $z \gg 1$. One possible way to estimate $I(z > 1)$ is via the use of Padé approximants [39]. However, they introduce both unphysical poles and an asymptotic behavior for $z \gg 1$ which may be unphysical. A recent better approximation method appears to be the use of hypergeometric functions [40, 41]. They do not have poles at finite z , their asymptotic behavior for $z \gg 1$ is reasonable, and they dispose a flexible and general character, as several functions are special cases of them. Specifically, we approximate

$$I_i(z) \simeq y_i \text{Re} \left\{ {}_2F_1(a_i, b_i, c_i, d_i z^2) \right\} \quad , \quad (61)$$

for both $i = 1, 2$ by the hypergeometric function

$${}_2F_1(a, b, c, d x) = \sum_{n=0}^{\infty} \frac{(a)_n (b)_n}{n! (c)_n} d^n x^n \quad , \quad (62)$$

where $(a)_n = a(a+1)\dots(a+n-1)$, $(a)_0 = 1$ and Re denotes the real part, as the conductivity we are interested in here is manifestly real (and ${}_2F_1(a, b, c, d x)$ for $d x > 1$ is complex in general, and given that the coefficients a_i and b_i turn out to be complex). The coefficients y_i adjust the overall scale as the first term of ${}_2F_1$ is 1. They are $y_1 = 4$ and $y_2 = 4/9$. We obtain the coefficients a_i, b_i, c_i, d_i by equating the coefficients of $y_i {}_2F_1$ and I_i for $n = 1 - 4$. Thus we have $a_1 = (2019 - i\sqrt{404039})/4600$, $b_1 = (2019 + i\sqrt{404039})/4600$, $c_1 = 1461/764$, $d_1 = 575/573$ and $a_2 = (11397 - 9i\sqrt{67191})/10976$, $b_2 = (11397 + 9i\sqrt{67191})/10976$, $c_2 = 17125/5464$, $d_2 = 2058/683$. We note that a_i and b_i are complex conjugate.

Plotting $zI(z)$ we see that the term $z^2 I_2(z)/\Lambda_u^4$ is much smaller than $I_1(z)$ and may be ignored. We see that $\max zI_1(z) \simeq 2.384$ for $z = 13$.

7. Overview

In this work we developed further our original diagrammatic model [18] for GMR, aiming to explain the XMR experiments already cited. Our model explains the salient features of XMR. Namely, the big magnitude of the effect as a function of the magnetic field H , its gradual decay with increasing temperature T , and its anisotropy as a function of the direction of H . The magnitude of XMR is higher in cleaner, i.e. less disordered, samples. As stated after eq. (46), for moderate H our mechanism may yield XMR linear in H , which for higher H may switch to H^b , $b \sim 2$ etc., in agreement with experiments. Overall, our mechanism acts in the bulk, *not* in the surface of the samples, and relies on a big conductivity for $H = 0$, which is quickly reduced with increasing H . All these are in good agreement with experiments. In section 6 we discussed the special role of Pt, Sc and Rh containing compounds.

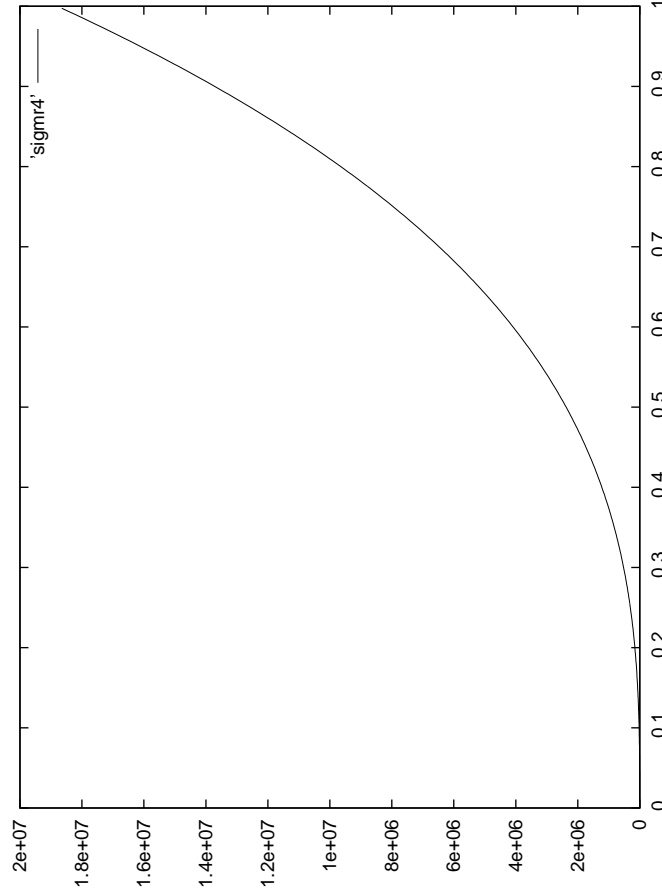


FIG. 15: Plot of $XMR = \rho(H)/\rho(0) - 1 = \sigma(0)/\sigma(H) - 1$ from eqs. (58),(57) as a function of the magnetic field H . In this figure XMR *exceeds* $1.8 \cdot 10^7$. For large enough H XMR saturates due to the decay of c_H in eq. (4). For the same reason XMR vanishes at elevated T .

A physical interpretation of XMR as a manifestation of quantum interference effects at the macroscopic scale is presented in section 5, after eq. (48).

* e-mail : kast@iesl.forth.gr ; giwkast@gmail.com

-
- [1] Mun E. et al., Phys. Rev. B **85**, (2012) 035135.
 - [2] H. Takatsu et al., Phys. Rev. Lett. **111**, (2013) 056601
 - [3] Ali, M. N. et al., Nature **514**, (2014) 205.
 - [4] Ali, M. N. et al., Europhys. Lett. **110**, (2015) 67002.
 - [5] Wang K. et al., Sci. Rep. **4**, (2014) 7328.
 - [6] Shekhar C. et al., Nat. Phys. **11**, (2015) 645.
 - [7] Wang Zh. et al., arXiv:1603.01717.
 - [8] Tafti, F.F. et al., Nat. Phys. **12**, (2016) 272.
 - [9] Zeng L.-K. et al., Phys. Rev. Lett. **117**, (2016) 127204.
 - [10] Tafti, F.F. et al., PNAS **113**, E3475 (2016).
 - [11] Zeng L.-K. et al., Phys. Rev. Lett. **117**, 127204 (2016); arXiv:1604.08142.
 - [12] Nayak J. et al., Nature Comm. **8**, 13942 (2017); arXiv:1605.06997.
 - [13] Chen F.C. et al., Phys. Rev. B **94**, 235154 (2016).
 - [14] Singha R., Pariari A., Satpati B., and Mandal P., PNAS **114**, 2468 (2017); arXiv:1602.01993.

- [15] Wang. X. et al., Adv. Electron. Mater. **2**, 1600228 (2016); arXiv:1604.00108.
- [16] Lv Y.-Y. et al., Appl. Phys. Lett. **108** (2016) 244101.
- [17] Gao W. et al., Phys. Rev. Lett. **118**, (2017) 256601 ; arXiv:1609.02626.
- [18] Kastinakis G., Europhys. Lett., **42** (1998) 345.
- [19] Schulze R., Phys. Zeit., **17** (1941) 297.
- [20] Tsui F, Uher C. and Flynn C.P., Phys. Rev. Lett., **72** (1994) 3084.
- [21] Tyler A.W. et al., Phys. Rev. B, **57** (1998) R728.
- [22] McKenzie R.H. et al., Phys. Rev. B, **57** (1998) 11854.
- [23] Rata A.D., Kataev V., Khomskii D., and Hibma T., Phys. Rev. B **68**, (2003) 220403.
- [24] Liang T. et al., Nature Mater., **14** (2015) 280.
- [25] Pavlosiuk O., Swatek P., Wisniewski P., Sci. Rep. **6**, 38691 (2016); arXiv:1604.06945.
- [26] Hou Z. et al., Appl. Phys. Lett. **107**, (2015) 202103.
- [27] Yang X. et al., Appl. Phys. Lett., **108** (2016) 252401.
- [28] Pramanick S., P Dutta, S Chatterjee, S. Giri and S. Majumdaret, J. Phys. D: Appl. Phys. **50**, 035006 (2016) ; arXiv:1610.06771.
- [29] Sultana R. et al., J. Magn. Mag. Mater **428**, 213 (2017); arXiv:1611.02859.
- [30] Lee P.A. and Ramakrishnan T.V., Rev. Mod. Phys. **57**, (1985) 287.
- [31] Kastinakis G., Physica B **387**, (2007) 109.
- [32] Sigalas M.M. and Papaconstantopoulos D.A., Phys. Rev. B **50**, (1994) 7255.
- [33] Kawabata A., J. Phys. Soc. Jap. **49**, (1980) 628.
- [34] Kastinakis G., Phys. Rev. B. **72**, (2005) 075137.
- [35] Abrikosov A. A., Gorkov L. P. and Dzyaloshinski I. E., Methods of Quantum Field Theory in Statistical Physics, Prentice-Hall (Cliffwoods, NY), (1964).
- [36] We give the first 16 g_n 's : $g_1 = -1, g_2 = 1, g_3 = 1, g_4 = -1, g_5 = -1, g_6 = 1, g_7 = 1, g_8 = -1, g_9 = -1, g_{10} = 1, g_{11} = 1, g_{12} = -1, g_{13} = -1, g_{14} = 1, g_{15} = 1, g_{16} = -1$, etc. g_n 's are periodic in n with a period $\Delta n = 4$.
- [37] The series $I_1(z)$ diverges for $z \rightarrow 1$.
- [38] Baym G., Phys. Rev. **127**, (1962) 1391.
- [39] Baker G.A. and Morris P.R., Padé Approximants (Cambridge University Press, Cambridge, 1996).
- [40] Mera H., Pedersen T.G. and Nikolić B.K., Phys. Rev. Lett. **115**, (2015) 143001 ; the method was introduced in this paper.
- [41] Sanders S., Heinisch C. and Holthaus M., EPL **111**, (2015) 2002.